Supplementary Material

Three factors make bulk high-entropy alloys as effective electrocatalysts for oxygen evolution

Tao Zhang[1,6], Hui-Feng Zhao[1,6], Ke-Yan Wang[3], Zhen-Jie Chen[4,5], Li Li[2], Jing Peng [4,5], Xu Peng [2,*], Yong-Jiang Huang [3,*] and Hai-Bin Yu[1,*]

[1] Wuhan National High Magnetic Field Center & School of Physic, Huazhong University of Science and Technology, Wuhan 430074, China

[2] College of Chemistry and Chemical Engineering, Hubei University, Wuhan 430062, China

[3] School of Materials Science and Engineering, Center of Analysis Measurement and Computing, Harbin Institute of Technology, Harbin 150001, China

[4] Faculty of Materials Science and Energy Engineering/Institute of Technology for Carbon Neutrality

[5] Shenzhen Key Laboratory of Energy Materials for Carbon Neutrality, Shenzhen Institutes of Advanced Technology, Chinese Academy of Sciences, Shenzhen, 518055, China

[6] These authors contributed equally to this work.

* Authors to whom any correspondence should be addressed.

E-mail: haibinyu@hust.edu.cn, pengxu@hubu.edu.cn and yjhuang@hit.edu.cn

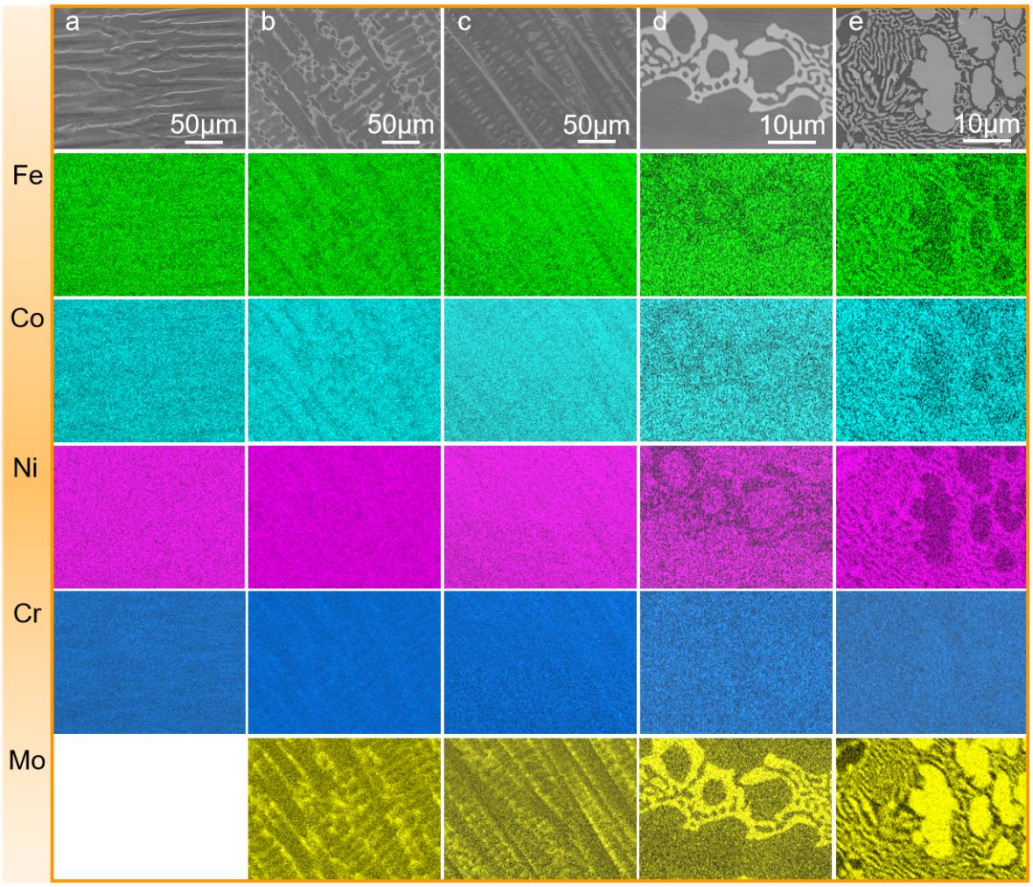

Figure S1. SEM images (top panel) and EDS elemental mapping. (a) CrFeCoNi; (b) $CrFeCoNiMo_{0.1}$; (c) $CrFeCoNiMo_{0.2}$; (d) $CrFeCoNiMo_{0.5}$; (e) CrFeCoNiMo. Note that: the non-uniform distribution in (b) and (c) is not caused by phase separation but by dendrites specific to the cast alloy. This structure is formed due to nonequilibrium cooling and does not change the f.c.c. structure.

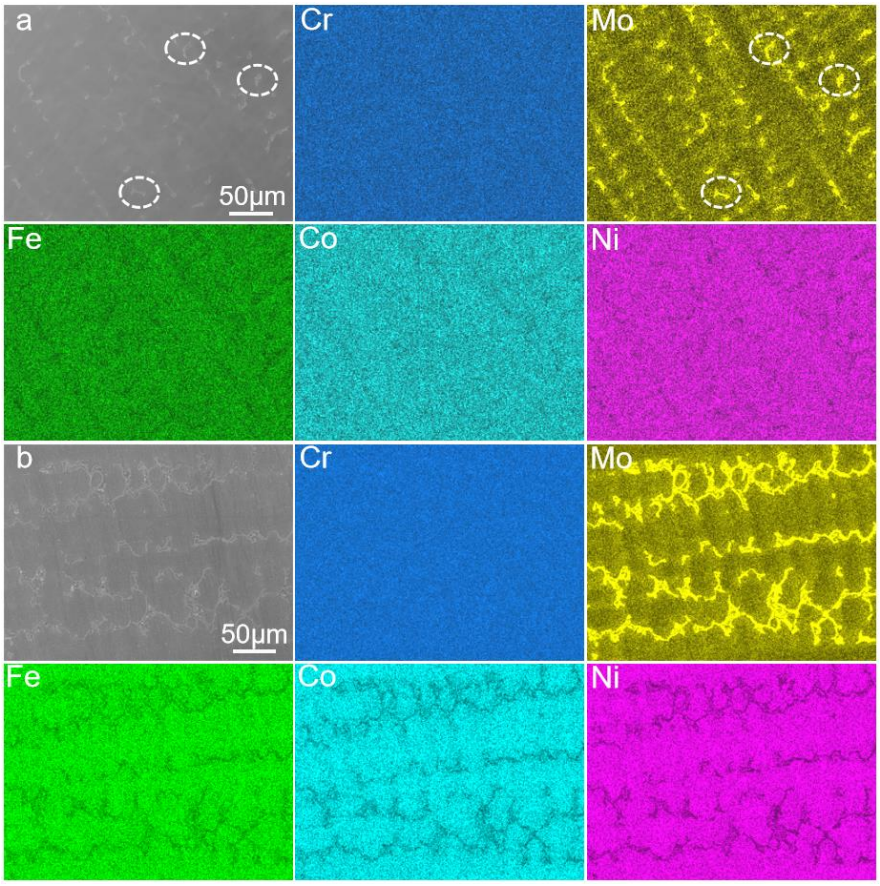

Figure S2. SEM images and EDS elemental mapping. (a) $CrFeCoNiMo_{0.3}$. The white dashed circles marked the μ phase. (b) $CrFeCoNiMo_{0.4}$. It follows that the excessive addition of Mo leads to an increase in the volume fraction of the μ phase.

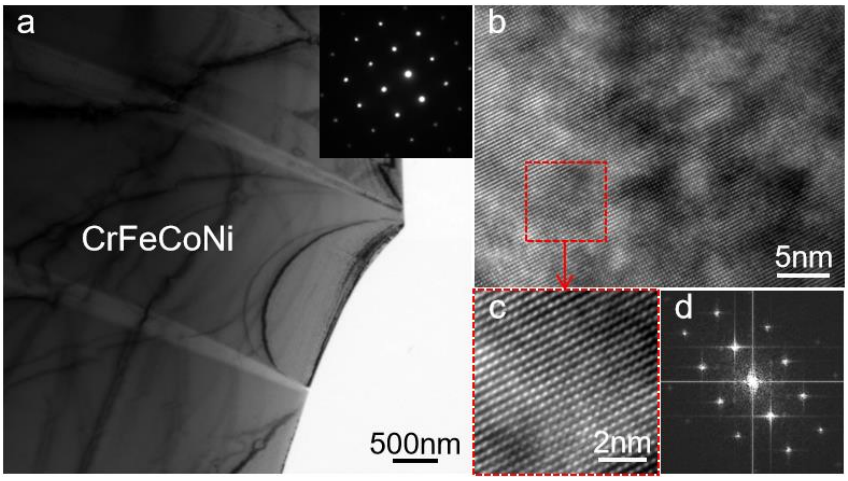

Figure S3. TEM images of CrFeCoNi HEA. (a) TEM bright-field image. The inset is the SAED pattern. (b) HRTEM image. (c) Magnified image of the red dashed box in (b). (d) is the FFT pattern of (c). The results indicate that the CrFeCoNi consisted of a single f.c.c. phase.

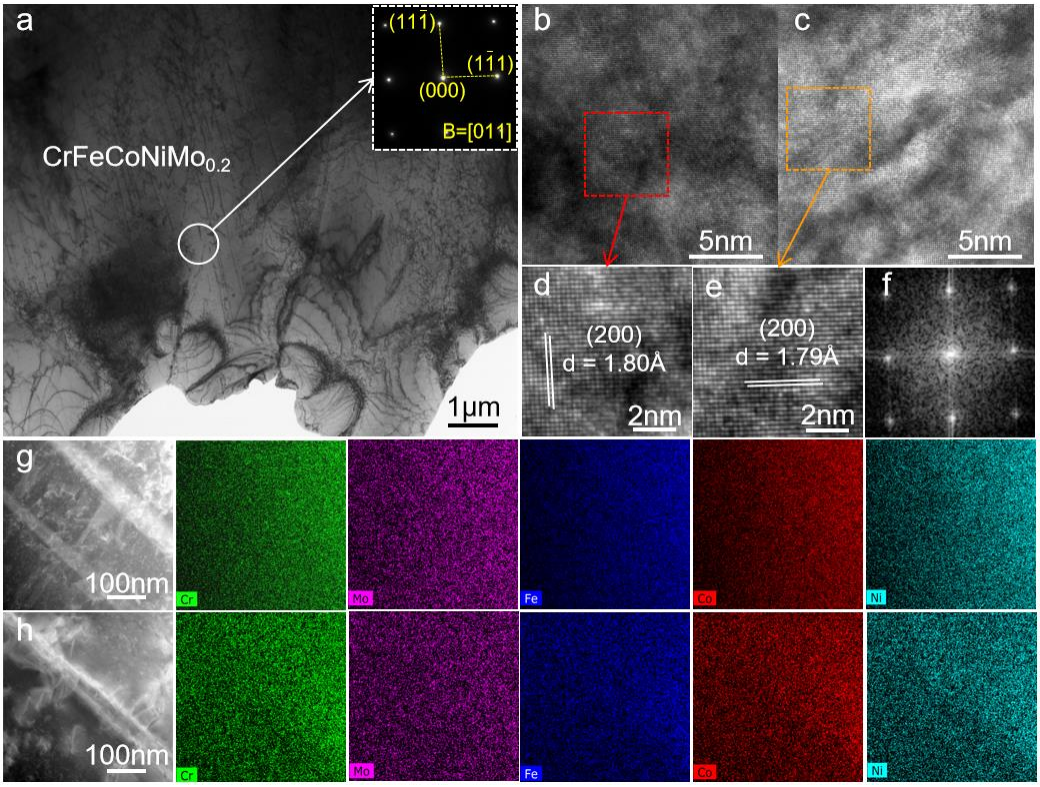

Figure S4. TEM images of $CrFeCoNiMo_{0.2}$ HEA. (a) TEM bright-field image. The inset is the SAED pattern. (b) and (c) are the HRTEM images of the regions with relatively high and low Mo content in the structure, respectively. (d) and (e) correspond to the enlarged HRTEM image in the red dashed and yellow dashed box in (b) and (c), respectively. f, is the FFT pattern of (d) and (e). Due to the identical FFT pattern of (d) and (e), only one is shown here. (g) and (h) are the HAADF-TEM images. (g) corresponds to high Mo content and (h) corresponds to low Mo contents.

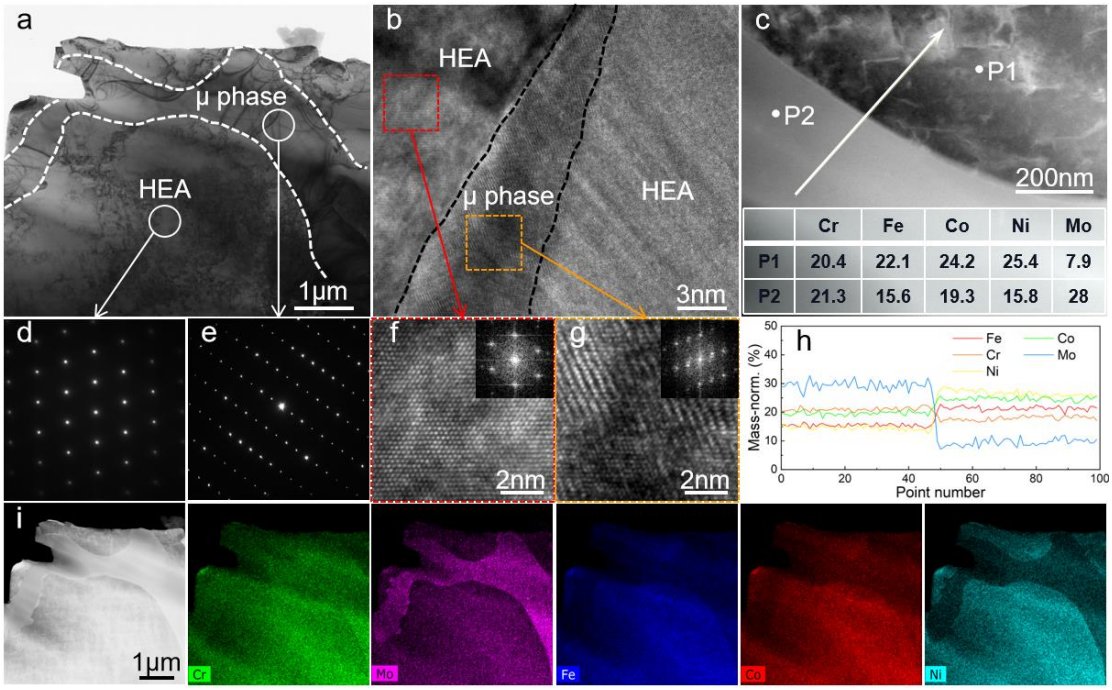

	Cr	Fe	Co	Ni	Mo
P1	20.4	22.1	24.2	25.4	7.9
P2	21.3	15.6	19.3	15.8	28

Figure S5. TEM images of CrFeCoNiMo HEA. (a) Microscopic morphology of the region containing the μ and f.c.c. phases. (b) HRTEM image. The interface between HEA and μ-phase is marked by the black dashed line. (c) TEM image at the interface between μ and f.c.c. phases. The table in (c) show the atomic ratios of Cr, Fe, Co, Ni, and Mo elements in μ and f.c.c. phases. (d) and (e) are the SAED patterns corresponding to μ and f.c.c. phase in (a), respectively. (f) and (g) are the enlargement of HRTEM images corresponding to μ and f.c.c. phase in (b), respectively. The inset both show the corresponding FFT patterns. (h) The EDX-line analysis of the white lines in (c). (i) TEM image and the corresponding elemental mappings of Cr, Fe, Co, Ni, Mo elements.

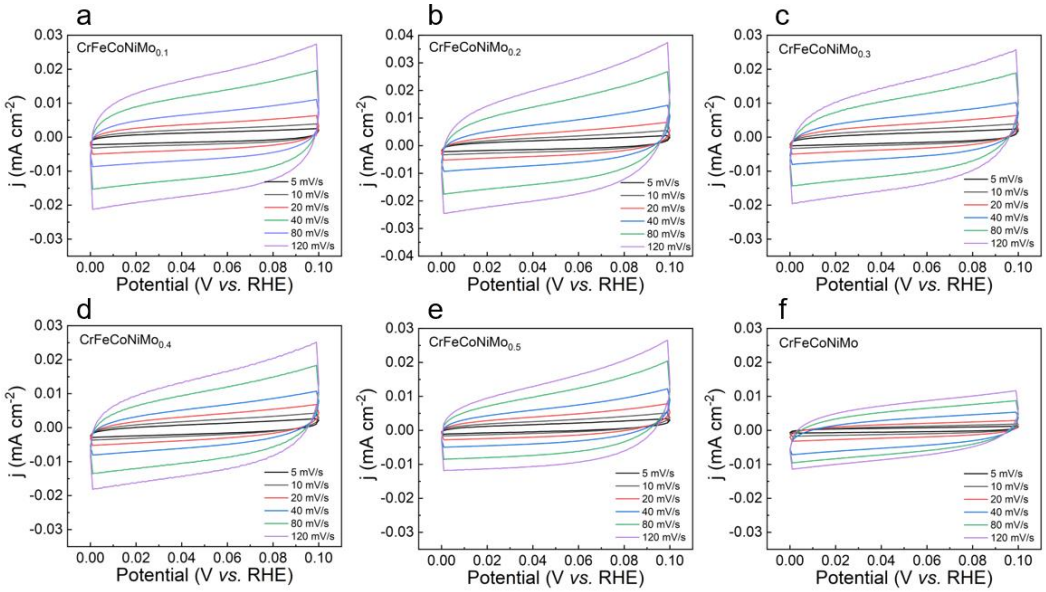

Figure S6. CV curves at different scan rates in the non-Faraday interval of 0-0.1 V. (a) $CrFeCoNiMo_{0.1}$. (b) $CrFeCoNiMo_{0.2}$. (c) $CrFeCoNiMo_{0.3}$. (d) $CrFeCoNiMo_{0.4}$. (e) $CrFeCoNiMo_{0.5}$. (f) CrFeCoNiMo. The scan rates are 5, 10, 20, 40, 80, 120 mV s^{-1}.

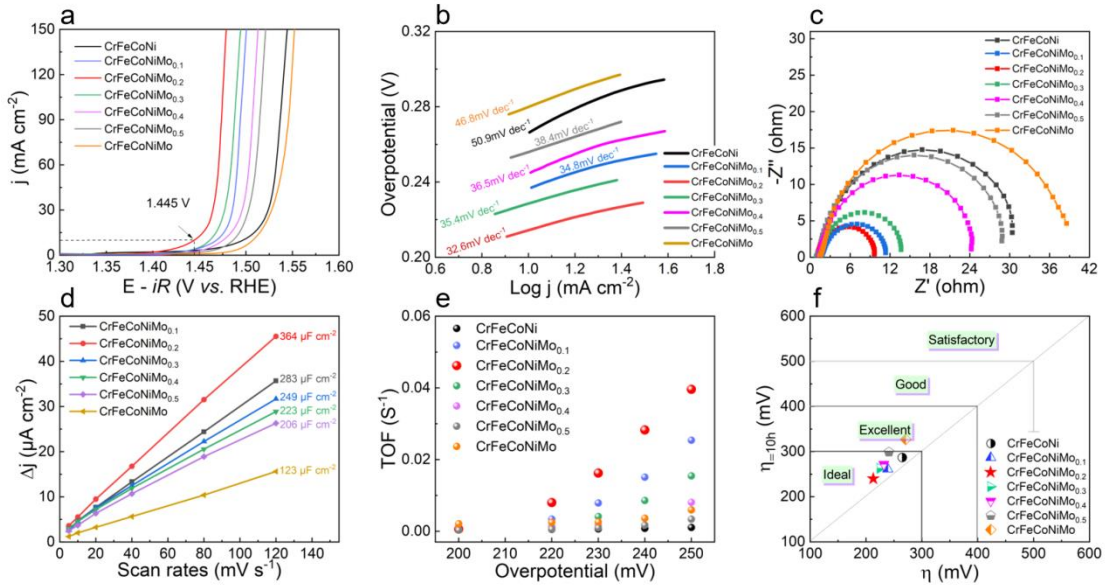

Figure S7. OER performance of $CrFeCoNiMo_x$. (a) OER polarization curves. (b) Tafel slopes. (c) EIS Nyquist plots. (d) C_{dl} curves. (e) TOF curves. (f) Classification of the HEAs based on OER performance.

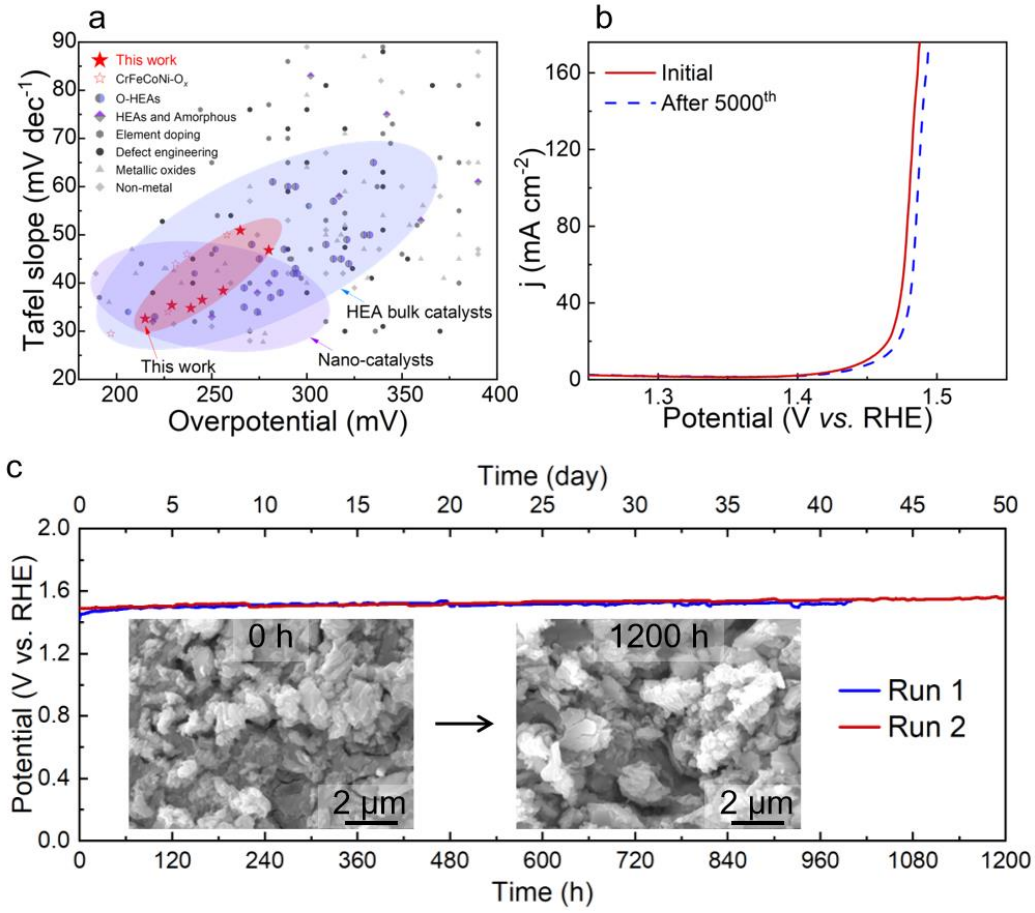

Figure S8. OER performance comparison and electrochemical stability. (a) The OER preformance comparison showing the overpotential at 10 mA cm^{-2} with Tafel slope in 1.0 M KOH. (b) OER polarization curves after 5000th CVs of CrFeCoNiMo$_{0.2}$ electrocatalyst. (c) Long-term stability testing of CrFeCoNiMo$_{0.2}$ at a constant current density of 10 mA cm^{-2}. The inset shows the SEM image of the surface after stability test.

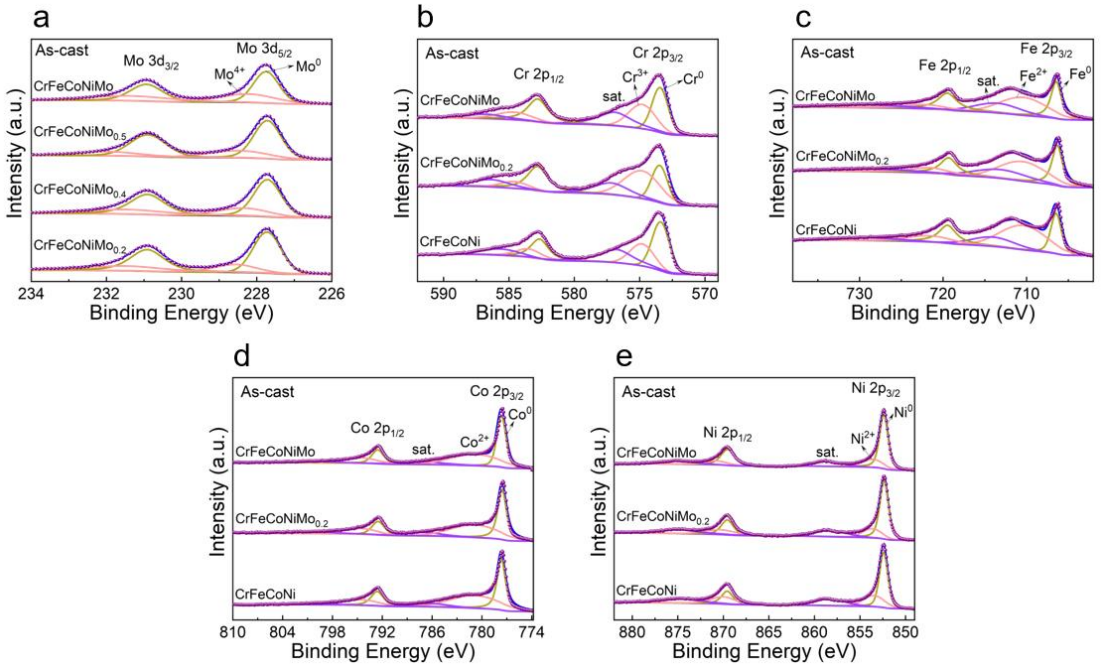

Figure S9. High-resolution XPS spectra of as-cast samples. (a) Mo 3d. (b) Cr 2p. (c) Fe 2p. (d) Co 2p. (e) Ni 2p.

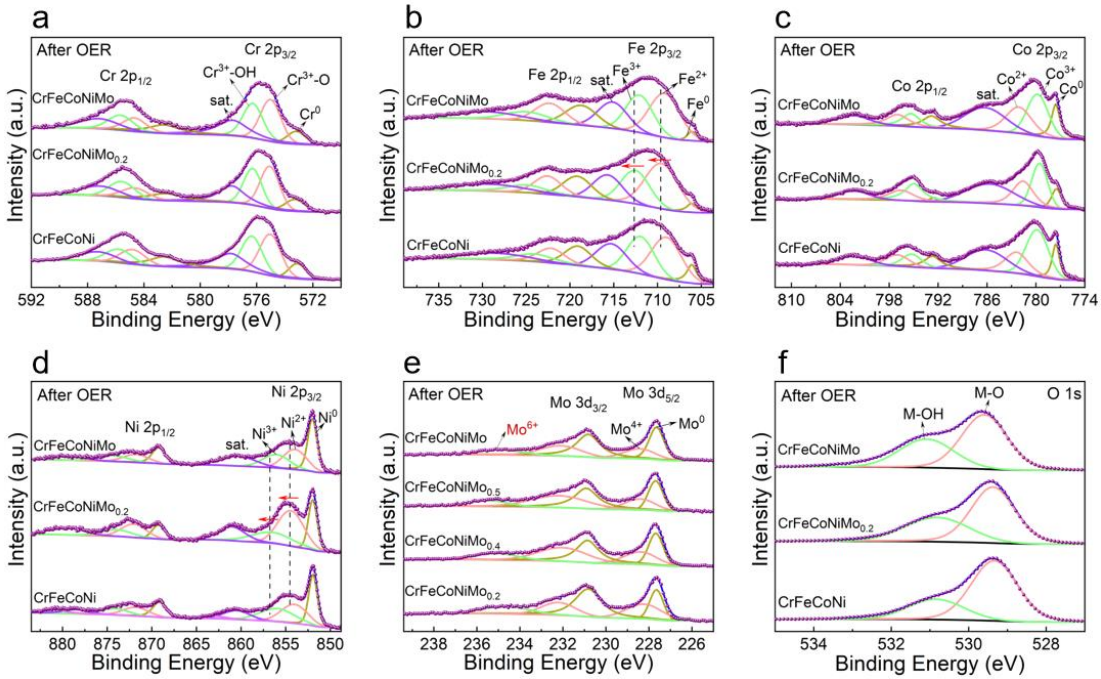

Figure S10. High-resolution XPS spectra after OER. (a) Cr 2p. (b) Fe 2p. (c) Co 2p. (d) Ni 2p. (e) Mo 3d. (f) O 1s.

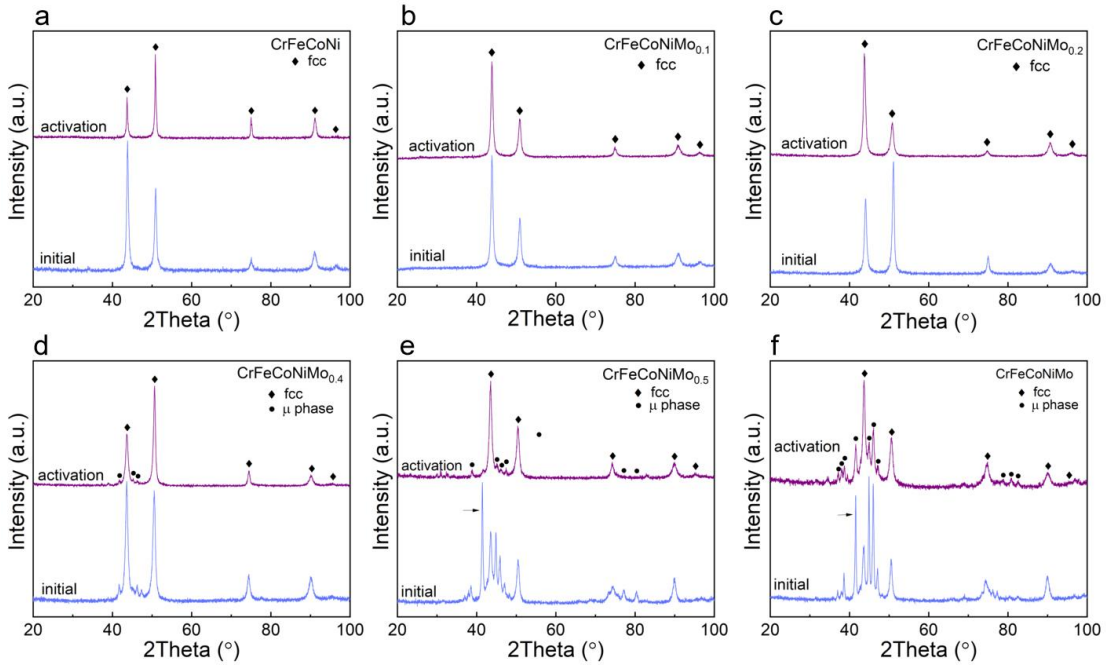

Figure S11. XRD patterns of CrFeCoNiMo$_x$ HEAs before and after electrochemical activition. (a) CrFeCoNi. (b) CrFeCoNiMo$_{0.1}$. (c) CrFeCoNiMo$_{0.2}$. (d) CrFeCoNiMo$_{0.4}$. (e) CrFeCoNiMo$_{0.5}$. (f) CrFeCoNiMo. The analysis of CrFeCoNiMo$_x$ (x = 0.4, 0.5, 1) show that the intensity of the diffraction peak corresponding to μ phase decreased after activition, indicating that the μ phase is corroded in alkaline solution.

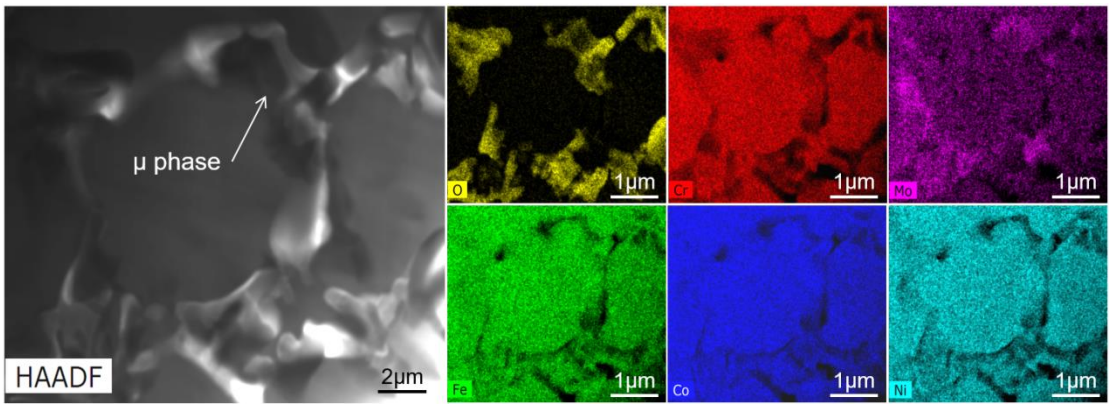

Figure S12. TEM-HAADF images of CrFeCoNiMo electrocatalysts after electrocatalytic. The Cr, Fe, Co, Ni and Mo elements in the μ phase show significant chemical shedding after OER testing. The content of O element on μ phase is much higher than on the substrate. It indicates that μ phase is corroded.

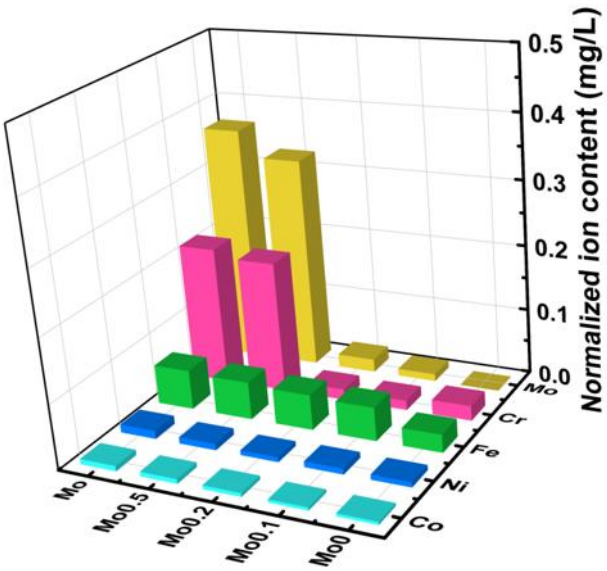

Figure S13. The ICP-OES results of each element in the electrolyte.

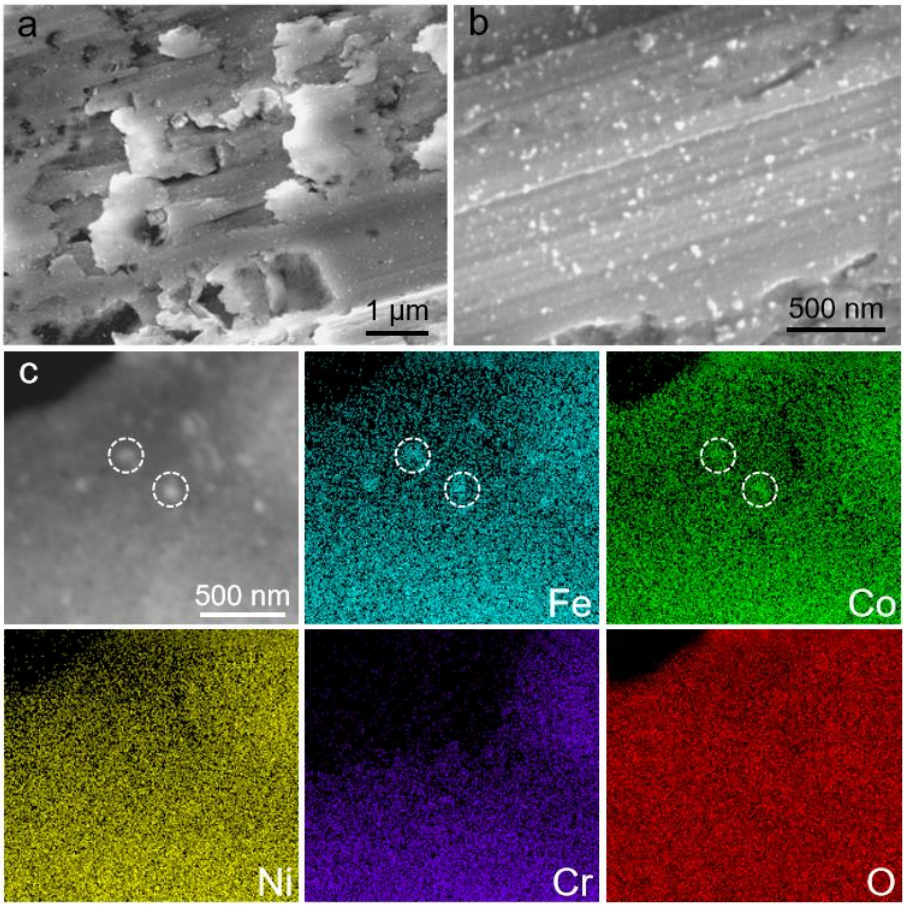

Figure S14. SEM and TEM images of CrFeCoNi after electrochemical activition. (a) and (b) are SEM images at different magnifications. The formation of nanoparticles on the catalyst surface can be clearly observed in (b). (c) TEM images and elemental mapping.

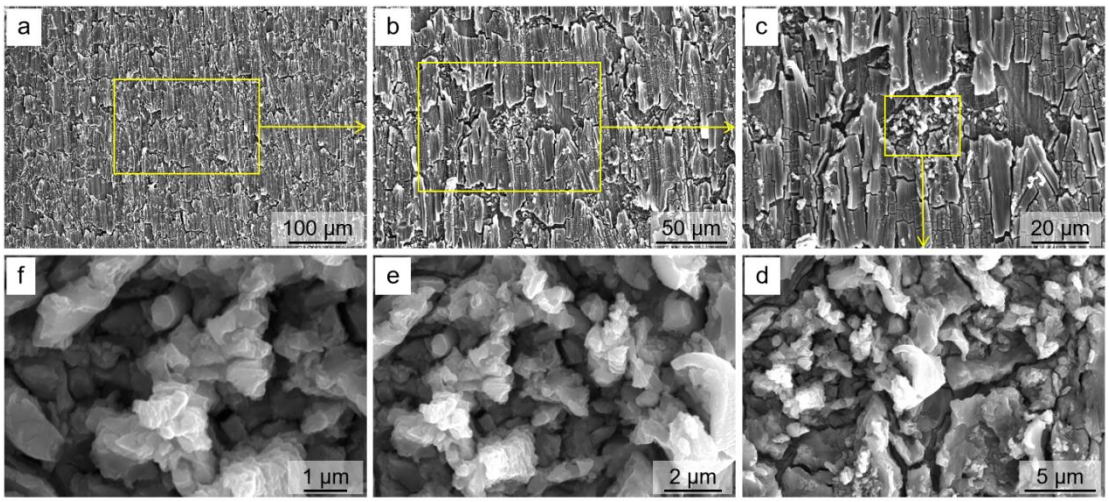

Figure S15. SEM images of $CrFeCoNiMo_{0.2}$ after electrochemical activition. From (a) to (f) is the stepwise amplification of the multi-metal oxide formed on the surface.

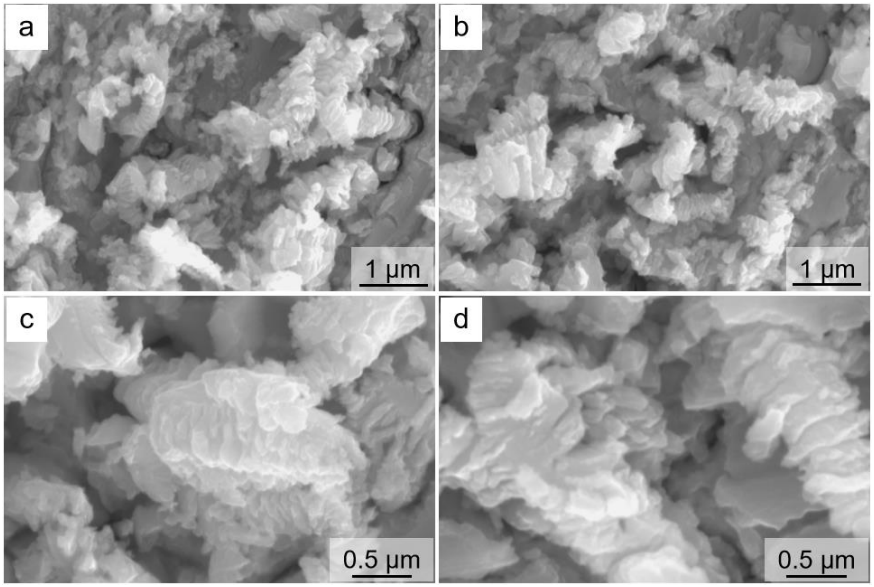

Figure S16. SEM images of the characteristic morphology of multi-metal oxides on the $CrFeCoNiMo_{0.2}$ surface.

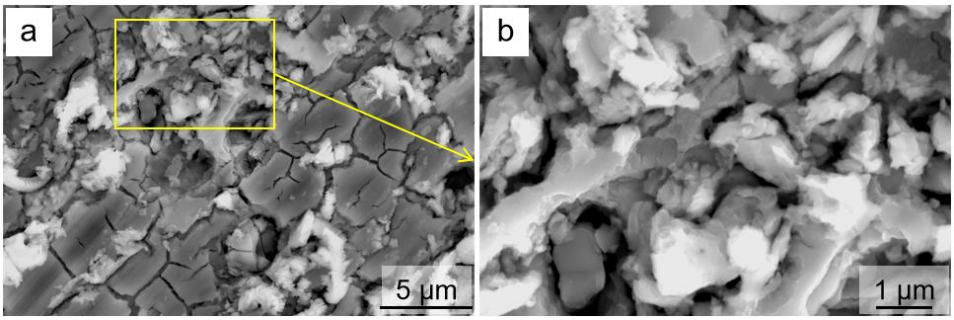

Figure S17. SEM images of oxides on the surface of CrFeCoNiMo. (a) Distribution of oxides on the surface. (b) Enlarged view of the yellow box in (a). Compared with $CrFeCoNiMo_{0.2}$, the oxide formed on the surface of CrFeCoNiMo is reduced and unshaped.

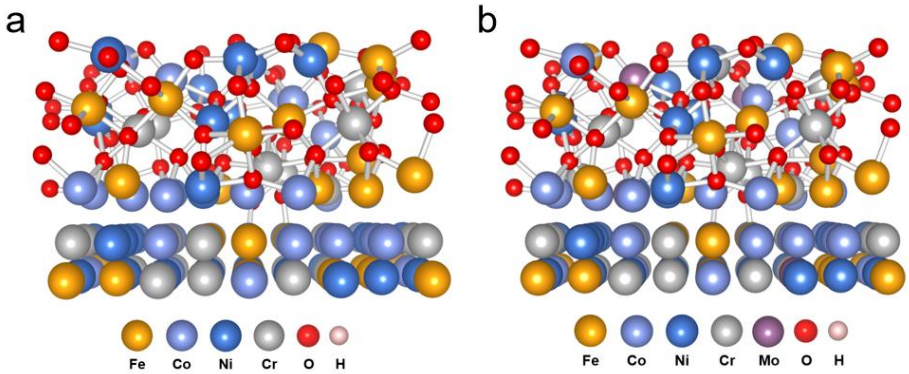

Figure S18. Optimized models considered for DFT calculations. (a) CrFeCoNi. (b) $CrFeCoNiMo_{0.2}$.

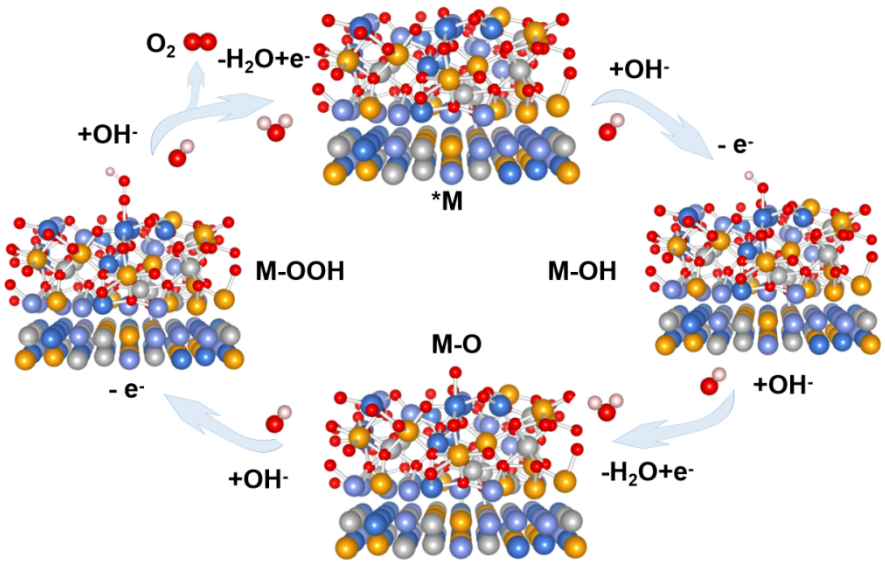

Figure S19. Multistep OER reactions on different atomic configurations of CrFeCoNi.

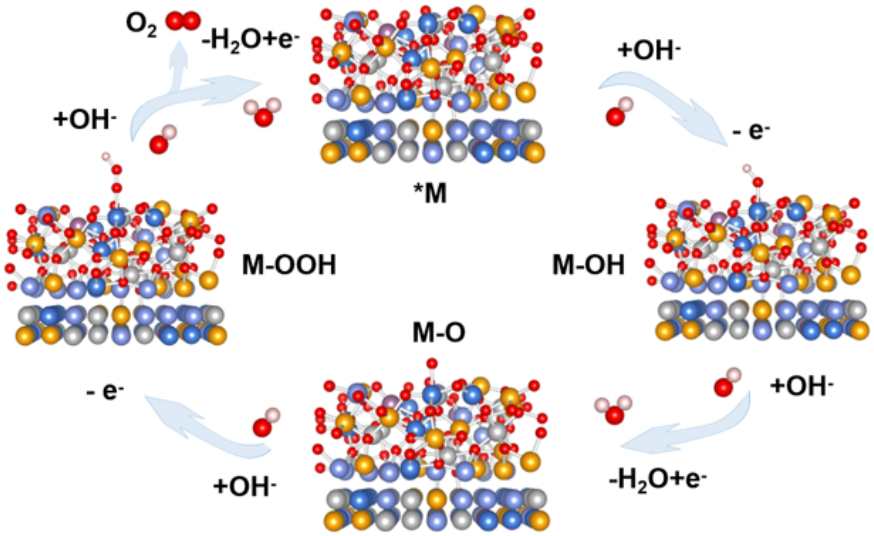

Figure S20. Multistep OER reactions on different atomic configurations of $CrFeCoNiMo_{0.2}$. The groups located in the upper part of the model are oxygen-containing intermediates

Table S1. The electrocatalytic OER performance of this work and the performance data reported for other catalysts, including high entropy materials, amorphous materials and containing high value metal materials.

Number	Catalyst	Substrate	Electrolyte	η (mV)	Tafel slope (mV dec^{-1})	Ref.
1	CrFeCoNi			265	50.9	
2	$CrFeCoNiMo_{0.1}$			239	34.8	
3	$CrFeCoNiMo_{0.2}$			215	32.6	
4	$CrFeCoNiMo_{0.3}$	Integrated	1.0 M KOH	229	35.4	This work
5	$CrFeCoNiMo_{0.4}$			245	36.5	
6	$CrFeCoNiMo_{0.5}$			256	38.4	
7	CrFeCoNiMo			280	46.8	
High-entropy materials						
8	Fe-Co-Ni-Cr-Nb	Self-supported	0.1 M KOH	288	27	[1]
9	FeCoCrNi			221	38.7	
10	FeCrNi	CCs	1.0 M KOH	255	42.6	[2]
11	CoCrNi			304	51.4	
12	$MnFeCoNi/MO_x$	Self-supported	1.0 M KOH	302	83.7	[3]
13	CoFeLaNiPt	HOPG/GC	0.1 M KOH	377		[4]
14	FeCoNiP			280 @ 100 mA cm^{-2}	60	
15	$FeCoNiP_{0.5}S_{0.5}$	Self-supported	1.0 M KOH	258 @ 100 mA cm^{-2}	49	[5]
16	FeCoNiS			300 @ 100 mA cm^{-2}	80	
17	AlNiCoRuMo			245	54.5	
18	AlNiCoRuCu	GC	1.0 M KOH	265	57	[6]
19	AlNiCoRu			270	68.3	
20	AlNiCoFeMo	Al precursor	1.0 M KOH	240	46	[7]

21	CoCrFeNiAl	Self-supported	1.0 M KOH	240	57	[8]
22	Co-Cu-Fe-Mo	Cu foil		199	48.8	
23	Co-Cu-Mo	Cu foil	1.0 M KOH	273	57.5	[9]
24	Co-Fe-Mo	CCC		253	51.2	
25	Al-Ni-Co-Ir-Mo	Al precursor	1.0 M KOH	233	55.2	[10]
26	CoCrFeMnNi	Self-supported	1.0 M NaOH			[11]
27	$(CoCuFeMnNi)_3O_4$	MWCNT	1.0 M KOH	350	59.5	[12]
28	FeNiMnCrCu	Self-supported	1.0 M NaOH	466 @ 40 mA cm^{-2}	58	[13]
29	FeCoNiCrAl			580 @ 40 mA cm^{-2}	75	
30	$(CrFeCoNi)_{97}O_3$			196	29	
31	$(CrFeCoNiCu)_{97}O_3$	Integrated	1.0 M KOH	211	27	[14]
32	$(CrFeCoNiMn)_{99}O_1$			271	35	
33	$(FeCoNi)_3O_{4-x}$	Self-supported	1.0 M KOH	229		[15]
34	FeCoNiMnCu	self-assembled		280	59	[16]
35	AlCoFeMoCr	GC	1.0 M KOH	260	52.4	[17]
36	FeCoNiMn			266	64.5	
37	FeCoNiSn	CFP	1.0 M KOH	264	68.2	[18]
38	FeCoNiCu			258	73.9	
39	FeVNbTiZrOF	CC	1.0 M KOH	348	110.3	[19]
40	$(CoNiMnZnFe)_3O_{3.2}$	CFP	1.0 M KOH	336	47.5	[20]
41	MnFeCoNiCu	CC	1.0 M KOH	263	43	[21]
42	CoFeNiMnMoPi	PTFE film	1.0 M KOH	270	74	[22]
43	$K_{0.8}Na_{0.2}(MgMnFeCoNi)F_3$			314	55	
44	$K(MgMnFeCoNi)F_3$	GC	1.0 M KOH	369	61	[23]
45	$Na(MgMnFeCoNi)F_3$			334	57	
Amorphous/glass materials						
46	NiFeP	Self-supported	1.0 M KOH	219	32	[24]
47	$Ni_{1.5}Sn@triMPO_4$	$triMPO_4$	1.0 M KOH	240	45.2	[25]
48	$(Fe_{73.5}Si_{13.5}B_9Nb_3Cu_1)_{91.5}Ni_{8.5}$	Self-supported	1.0 M KOH	230	130	[26]
49	$Fe_{40}Ni_{20}Co_{20}P_{15}C_5$	Self-supported	1.0 M KOH	278	40	[27]
50	$Ni_{40}Fe_{40}P_{20}$			270	35	
51	$Ni_{70}Pd_{10}P_{20}$	Self-supported	1.0 M KOH	345	42	[28]
52	$Ni_{40}Pd_{40}P_{20}$			340	46	
53	Ni-Fe-P	Cu foil	30 wt.% KOH	309	79.4	[29]
Containing high valance metal materials						
54	NiFeMo	Ni foam	1.0 M KOH	220	35	[30]
55	$(Ni_xFe_yCo_{6-x-y})Mo_6C$	Ni foam	1.0 M KOH	212	55.1	[31]
56	FeCoMoS	NG	1.0 M KOH	238	51	[32]
57	CoMoS			300	77	
58	FeCoMo	GC	1.0 M KOH	277	27.7	[33]
69	NiFe-MoO_x	Self-supported	1.0 M KOH	276	55	[34]
60	$Co@WC_{1-x}$	NCNTs	0.1 M KOH	330	90	[35]
61	Mo-CoP	CC	1.0 M KOH	305	56	[36]
62	FeCoMoW	CP/Ni foam	1.0 M KOH	212		[37]
63	NiFeMoW			205		
64	NiFeMo			201		
65	NiFeW			202		
66	G-FeCoW	Au foam	1.0 M KOH	191		[38]
67	A-FeCoW			232		

68	FeNi-Mo_2C	carbon layers	1.0 M KOH	288	38.8	[39]
79	$Co_{0.76}Fe_{0.18}Mo_{0.06}O_{1.35}$	GC	1.0 M KOH	250	57	[40]
70	Fe-Mo-Te	GC	1.0 M KOH	300	45.6	[41]
71	P/Mo-Co_3O_4	CC	1.0 M KOH	265		[42]

Note: Unless otherwise denoted, the overpotential in the table corresponds to a current density of 10 mA cm^{-2}.

Supplementary References

[1] Ding Z Y, Bian J, Shuang S, Liu X D, Hu Y C, Sun C W, Yang Y 2020 High entropy intermetallic-oxide core-shell nanostructure as superb oxygen evolution reaction catalyst *Adv. Sustain. Syst.* **4** 1900105.

[2] Zhang N, Feng X, Rao D, Deng X, Cai L, Qiu B, Long R, Xiong Y, Lu Y, Chai Y 2020 Lattice oxygen activation enabled by high-valence metal sites for enhanced water oxidation *Nat. Commun.* **11** 4066.

[3] Dai W, Lu T, Pan Y 2019 Novel and promising electrocatalyst for oxygen evolution reaction based on MnFeCoNi high entropy alloy *J. Power Sources* **430** 104-111.

[4] Glasscott M W, Pendergast A D, Goines S, Bishop A R, Hoang A T, Renault C, Dick J E 2019 Electrosynthesis of high-entropy metallic glass nanoparticles for designer, multi-functional electrocatalysis *Nat. Commun.* **10** 2650.

[5] Wang X, Ma W, Ding C, Xu Z, Wang H, Zong X, Li C 2018 Amorphous multi-elements electrocatalysts with tunable bifunctionality toward overall water splitting *ACS Catal.* **8** 9926-9935.

[6] Jin Z Y, Lyu J, Zhao Y L, Li H L, Lin X, Xie G Q, Liu X J, Kai J J, Qiu H J 2020 Rugged high-entropy alloy nanowires with in situ formed surface spinel oxide as highly stable electrocatalyst in Zn-air batteries *ACS Mater. Lett.* **2** 1698-1706.

[7] Qiu H J, Fang G, Gao J, Wen Y R, Lv J, Li H L, Xie G Q, Liu X J, Sun S H 2019 Noble metal-free nanoporous high-entropy alloys as highly efficient electrocatalysts for oxygen evolution reaction *ACS Mater. Lett.* **1** 526-533.

[8] Ma P, Zhang S, Zhang M, Gu J, Zhang L, Sun Y, Ji W, Fu Z 2020 Hydroxylated high-entropy alloy as highly efficient catalyst for electrochemical oxygen evolution reaction *Sci. China Mater.* **63** 2613-2619.

[9] Zhang L, Cai W, Bao N 2021 Top-level design strategy to construct an advanced high-entropy Co-Cu-Fe-Mo (Oxy)hydroxide electrocatalyst for the oxygen evolution reaction *Adv. Mater.* **33** 2100745.

[10] Jin Z, Lv J, Jia H, Liu W, Li H, Chen Z, Lin X, Xie G, Liu X, Sun S, Qiu H J 2019 Nanoporous Al-Ni-Co-Ir-Mo high-entropy alloy for record-high water splitting activity in acidic environments *Small* **15** 1904180.

[11] Waag F, Li Y, Ziefuß A R, Bertin E, Kamp M, Duppel V, Marzun G, Kienle L, Barcikowski S, Gökce B 2019 Kinetically-controlled laser-synthesis of colloidal high-entropy alloy nanoparticles *RSC Adv.* **9** 18547-18558.

[12] Wang D, Liu Z J, Du S Q, Zhang Y Q, Li H, Xiao Z H, Chen W, Chen R, Wang Y Y, Zou Y Q, Wang S Y 2019 Low-temperature synthesis of small-sized high-entropy oxides for water oxidation *J. Mater. Chem. A* **7** 24211-24216.

[13] Cui X, Zhang B, Zeng C, Guo S 2018 Electrocatalytic activity of high-entropy alloys toward oxygen evolution reaction *MRS Commun.* **8** 1230-1235.

[14] Chen Z J, Zhang T, Gao X Y, Huang Y J, Qin X H, Wang Y F, Zhao K, Peng X, Zhang C, Liu L, Zeng M H, Yu H B 2021 Engineering microdomains of oxides in high-entropy alloy electrodes toward efficient oxygen evolution *Adv. Mater.* **33** 2101845.

[15] Wei R, Zhang K, Zhao P, An Y, Tang C, Chen C, Li X, Ma X, Ma Y, Hao X 2021 Defect-rich FeCoNiPB/$(FeCoNi)_3O_{4-x}$ high-entropy composite nanoparticles for oxygen evolution reaction: Impact of surface activation *Appl. Surface Sci.* **549** 149327.

[16] Huang K, Peng D, Yao Z X, Xia J Y, Zhang B W, Liu H, Chen Z B, Wu F, Wu J S, Huang Y Z 2021 Cathodic plasma driven self-assembly of HEAs dendrites by pure single FCC FeCoNiMnCu nanoparticles as high efficient electrocatalysts for OER *Chem. Eng. J.* **425** 131533.

[17] Jin Z, Lyu J, Zhao Y-L, Li H, Chen Z, Lin X, Xie G, Liu X, Kai J-J, Qiu H-J 2021 Top-down synthesis of noble metal particles on high-entropy oxide supports for electrocatalysis *Chem. Mater.* **33** 1771-1780.

[18] Jiang S, Tian K, Li X, Duan C, Wang D, Wang Z, Sun H, Zheng R, Liu Y 2021 Amorphous high-entropy non-precious metal oxides with surface reconstruction toward highly efficient and durable catalyst for oxygen evolution reaction *J. Colloid Interface Sci.* **606** 635-644.

[19] Zhu Y, Dai W, Zhong X, Lu T, Pan Y 2021 In-situ reconstruction of non-noble multi-metal core-shell oxyfluorides for water oxidation *J. Colloid Interface Sci.* **602** 55-63.

[20] Zhang Y, Dai W, Zhang P, Lu T, Pan Y 2021 In-situ electrochemical tuning of $(CoNiMnZnFe)_3O_{3.2}$ high-entropy oxide for efficient oxygen evolution reactions *J. Alloy Compd.* **868** 159064.

[21] Huang K, Zhang B W, Wu J S, Zhang T Y, Peng D, Cao X, Zhang Z, Li Z, Huang Y Z 2020 Exploring the impact of atomic lattice deformation on oxygen evolution reactions based on a sub-5 nm pure face-centred cubic high-entropy alloy electrocatalyst *J. Mater. Chem. A* **8** 11938-11947.

[22] Qiao H, Wang X, Dong Q, Zheng H, Chen G, Hong M, Yang C-P, Wu M, He K, Hu L 2021 A high-entropy phosphate catalyst for oxygen evolution reaction *Nano Energy* **86** 106029.

[23] Wang T, Chen H, Yang Z, Liang J, Dai S 2020 High-entropy perovskite fluorides: A new platform for oxygen evolution catalysis *J. Am. Chem. Soc.* **142** 4550-4554.

[24] Hu F, Zhu S, Chen S, Li Y, Ma L, Wu T, Zhang Y, Wang C, Liu C, Yang X, Song L, Yang X, Xiong Y 2017 Amorphous metallic NiFeP: A conductive bulk material achieving high activity for oxygen evolution reaction in both alkaline and acidic media *Adv. Mater.* **29** 1606570.

[25] Li S, Li Z, Ma R, Gao C, Liu L, Hu L, Zhu J, Sun T, Tang Y, Liu D, Wang J 2021 A glass-ceramic with accelerated surface reconstruction toward the efficient oxygen evolution reaction *Angew. Chem. Int. Ed.* **60** 3773-3780.

[26] Chen S-Q, Li M, Ji Q, Chen X, Lan S, Feng T, Yao K-F 2021 Functional 3D nanoporous Fe-based alloy from metallic glass for high-efficiency water splitting and wastewater treatment *J. Non-Cryst. Solids* **571** 121070.

[27] Aneeshkumar K S, Tseng J-c, Liu X, Tian J, Diao D, Shen J 2021 Electrochemically dealloyed nanoporous $Fe_{40}Ni_{20}Co_{20}P_{15}C_5$ metallic glass for efficient and stable electrocatalytic hydrogen and oxygen generation *RSC Adv.* **11** 7369-7380.

[28] Tan Y, Zhu F, Wang H, Tian Y, Hirata A, Fujita T, Chen M 2017 Noble-metal-free metallic glass as a highly active and stable bifunctional electrocatalyst for water splitting *Adv. Mater. Interfaces* **4** 1601086.

[29] Lian J, Wu Y, Zhang H, Gu S, Zeng Z, Ye X 2018 One-step synthesis of amorphous Ni-Fe-P alloy as bifunctional electrocatalyst for overall water splitting in alkaline medium *Int. J. Hydrogen Energy* **43** 12929-12938.

[30] Qin F, Zhao Z H, Alam M K, Ni Y, Robles-Hernandez F, Yu L, Chen S, Ren Z F, Wang Z M, Bao J M 2018 Trimetallic NiFeMo for overall electrochemical water splitting with a low cell voltage *ACS Energy Lett.* **3** 546-554.

[31] He L-G, Cheng P-Y, Cheng C-C, Huang C-L, Hsieh C-T, Lu S-Y 2021 $(Ni_xFe_yCo_{6-x-y})Mo_6C$ cuboids as outstanding bifunctional electrocatalysts for overall water splitting *Appl. Catal. B* **290** 120049.

[32] Ramakrishnan S, Balamurugan J, Vinothkannan M, Kim A R, Sengodan S, Yoo D J 2020 Nitrogen-doped graphene encapsulated FeCoMoS nanoparticles as advanced trifunctional catalyst for water splitting devices and zinc-air batteries *Appl. Catal. B* **279** 119381.

[33] Liu P F, Yang S, Zheng L R, Zhang B, Yang H G 2017 Mo^{6+} activated multimetal oxygen-evolving catalysts *Chem. Sci.* **8** 3484-3488.

[34] Xie C, Wang Y, Hu K, Tao L, Huang X, Huo J, Wang S 2017 In situ confined synthesis of molybdenum oxide decorated nickel-iron alloy nanosheets from MoO_4^{2-} intercalated layered double hydroxides for the oxygen evolution reaction *J. Mater. Chem. A* **5** 87-91.

[35] Cai J, Zhang X, Yang M, Shi Y, Liu W, Lin S 2021 Constructing Co@WC_{1-x} heterostructure on N-doped carbon nanotubes as an efficient bifunctional electrocatalyst for zinc-air batteries *J. Power Sources* **485** 229251.

[36] Guan C, Xiao W, Wu H, Liu X, Zang W, Zhang H, Ding J, Feng Y P, Pennycook S J, Wang J 2018 Hollow Mo-doped CoP nanoarrays for efficient overall water splitting *Nano Energy* **48** 73-80.

[37] Zhang B, Wang L, Cao Z, Kozlov S M, García de Arquer F P, Dinh C T, Li J, Wang Z, Zheng X, Zhang L, Wen Y, Voznyy O, Comin R, De Luna P, Regier T, Bi W, Alp E E, Pao C-W, Zheng L, Hu Y, Ji Y, Li Y, Zhang Y, Cavallo L, Peng H, Sargent E H 2020 High-valence metals improve oxygen evolution reaction performance by modulating 3d metal oxidation cycle energetics *Nat. Catal.* **3** 985-992.

[38] Zhang B, Zheng X, Voznyy O, Comin R, Bajdich M, Garcia-Melchor M, Han L, Xu J, Liu M, Zheng L, Garcia de Arquer F P, Dinh C T, Fan F, Yuan M, Yassitepe E, Chen N, Regier T, Liu P, Li Y, De Luna P, Janmohamed A, Xin H L, Yang H, Vojvodic A, Sargent E H 2016 Homogeneously dispersed multimetal oxygen-evolving catalysts *Science* **352** 333-337.

[39] Wang M, Wang Y, Mao S S, Shen S 2021 Transition-metal alloy electrocatalysts with active sites modulated by metal-carbide heterophases for efficient oxygen evolution *Nano Energy* **88** 106216.

[40] Song S, Sun J, Zhou J, Hu Z, Lin H-J, Chan T-S, Chen C-T, Zhang N, Jing C, Hu J, Zhang L, Wang J-Q 2021 Unexpected increasing Co valence state of an exsolved catalyst by Mo doping for enhanced oxygen evolution reaction *Chem. Eng. J.* **425** 130681.

[41] He R, Li M, Qiao W, Feng L 2021 Fe doped Mo/Te nanorods with improved

stability for oxygen evolution reaction *Chem. Eng. J.* **423** 130168.
[42] Li R, Hu B, Yu T, Chen H, Wang Y, Song S 2020 Insights into correlation among surface-structure-activity of cobalt-derived pre-catalyst for oxygen evolution reaction *Adv. Sci.* **7** 1902830.